ARTICLE

Employing photoluminescence to rapidly follow aggregation and dispersion of cellulose nanofibrils

Received 00th January 20xx,
Accepted 00th January 20xx

DOI: 10.1039/x0xx00000x

Marcus A. Johns,[a]* Anna E. Lewandowska,[a]† Ellen Green,[b] Stephen J. Eichhorn[a]**

Photoluminescence of cellulose, and other polysaccharides, has long been presumed to be due to contamination of the material by other autofluorescent compounds – such as lignin, or proteins. This is attributed to the lack of known fluorescent chemical groups present in the molecular structure of polysaccharides and the weak emission intensity when compared to typical fluorophores. However, recent research suggests that the observed luminescence may actually be due to transitions involving the n orbitals containing lone electron pairs present in oxyl groups, stabilised by the molecular forces between the polysaccharide chains. Here we investigate this theory further by varying the physicochemical environment (concentration and pH) of oxidised cellulose nanofibril suspensions and observing the resultant fluorescent spectra using multi-channel confocal laser scanning spectroscopy. We confirm that both factors affect the material photoluminescence, specifically changing the intensity ratio between two localised emission maxima, supporting current theories. Furthermore, we demonstrate that this variation enables the determination of critical aggregation concentrations and the apparent pKa values of hydroxyl groups that undergo deprotonation within the examined pH range, enabling use of the technique to track rapid changes in the fibril physicochemical environment.

Introduction

Cellulose nanomaterials (CNMs) are a class of sustainable materials that may be derived from wood, plant, algae, bacterial and tunicate sources.[1] They are generally divided into two subcategories, nanocrystals (CNCs) and nanofibrils (CNFs), that are physically distinguished by differences in crystallinity and aspect ratio. CNFs generally have higher aspect ratios and lower crystallinity values than CNCs.[2] Their high specific Young's modulus, calculated to be around 85 N m g^{-1} for CNCs and 65 N m g^{-1} for CNFs;[3] sustainable sources; ease of functionalization and biocompatibility have resulted in their use for an array of potential applications.[1,2] These vary from composites and packaging,[4-9] to drug delivery,[10, 11] tissue engineering[12] and food additives[13] with final forms including films, textile fibres, and gels.

Unmodified CNMs will readily suspend in water-based systems due to their nanoscale dimensions. However, they will also aggregate together and precipitate from the formed suspensions and gels due to the lack of surface charge and propensity of cellulose to form hydrogen bonds with itself.[14] Therefore, chemical groups are introduced to the CNM surfaces to inhibit this aggregation, the most common method for which involves the introduction of ionic groups. This is readily achieved for CNCs by using an acid with at least two pKa values during the hydrolysis production step. Sulfuric acid, which introduces sulfate half-esters to the CNC surface,[2,15-17] is typically used due to its high pKa value although it has also been demonstrated for hydrobromic,[18] phosphoric,[19-21] and di- and tri-carboxylic (citric, malic, maleic, malonic, oxalic) acids.[22-24] CNFs, on the other hand, are commonly modified via 2,2,6,6-tetramethyl-piperidine-1-oxyl radical (TEMPO)-mediated oxidation to introduce carboxyl groups to the surface.[2, 25, 26]

The autofluorescence of poly- and oligo-saccharides, from various sources, has previously been widely reported.[6, 27-35] This autofluorescence is generally attributed to contamination of the sample with aromatic compounds, i.e. lignin, or proteins, dependent on the source.[36] However, the autofluorescence of materials without aromatic groups, including synthetic and natural polymers and amino acids, is being increasingly described,[37] which suggests that the luminescent property is inherent to the polymer. In relation to polysaccharides, Gong *et al.* hypothesised that the clustering of groups with lone pair electrons, such as the oxygen atoms in hydroxyl and carboxyl groups, results in electron cloud overlaps that are responsible for the luminescent properties of carbohydrate molecules.[29] The inter- and intramolecular force network between the chains

[a] *Department of Aerospace Engineering, Bristol Composites Institute (ACCIS), University of Bristol, Queens Building, University Walk, Bristol BS8 1TR, UK*
[b] *College of Engineering, Mathematics and Physical Sciences, University of Exeter, Exeter EX4 4QL, UK*
† Present address: Renishaw, Spectroscopy Products Division, New Mills, Wotton-under-Edge, Gloucestershire, GL12 8JR, UK (A.E.L.)

Electronic Supplementary Information (ESI) available: Figure demonstrating effect of OCNF concentration on presence of liquid crystal domains via cross-polarised light microscopy; Figure demonstrating effect of HCl and NaOH concentration on ζ-potential; Figure demonstrating effect of pH on ζ-potential; Figure demonstrating effect of pH on interfibrillar spacing determined by SAXS; Figure demonstrating effect of pH on Raman spectroscopy; Figure demonstrating effect of pH on rheology; Figure demonstrating effect of pH on OCNF autofluorescence, confirming aggregation at low pH; Figure tracking fluorescent emission intensity against pH; Tables providing equations for fitted exponential curves for each technique; Tables reporting interfibrillar spacing lengths and percentage contribution determined from SAXS. Video of OCNF macrofibre expansion obtained using MCLSS. Data access statement. See DOI: 10.1039/x0xx00000x

rigidify the molecular confirmations, block vibrational dissipation, and ensure emission.[29] The groups of Yuan and Zhang have used single crystal data to confirm that interconnected short (sub van der Waal radii) oxygen-oxygen contacts exist between D-glucose molecules,[38] as well as other monosaccharide units,[39] supporting this theory. We previously took advantage of this phenomenon to track the dispersion of cellulose particles in polymer matrices, confirming that the observed autofluorescence was intrinsically linked to the presence of cellulose.[6,31]

In relation to cellulosic nanomaterials with typical surface chemical modifications, Li *et al.* investigated the autofluorescent properties of carboxymethylated nanocellulose.[33] They demonstrated that the particles exhibited two fluorescent bands with an approximate wavelength difference of 40 nm, the second of which increased with concentration. This second peak was attributed to electron transitions between oxygen n orbitals and the carboxyl π* orbitals.[33] More recently, we tracked changes in the fluorescence of sulfated and hydrophobically-modified CNCs with an increase in concentration. We confirmed that the intensity ratio between the two observed bands, centred at 468 and 504 nm, and attributed to intra- and inter-particle molecular forces respectively, was concentration dependent, enabling a prediction of the critical aggregation concentration (CAC).[35]

Here we investigate the effects of concentration and protonation on the autofluorescence of oxidised CNFs (OCNFs). We demonstrate that the ratio between the two previously reported bands are impacted by both phenomena and support our previous assumptions. This enables the rapid determination of the CAC and apparent pKa values for cellulose nanofibril systems. To demonstrate the analytical potential of the technique, we track the 'real time' changes in autofluorescence during the dispersion of an OCNF macrofiber, confirming the roles of both concentration and protonation.

Experimental

Materials

Oxidized cellulose nanofibrils (OCNFs) (4 wt.% aqueous suspension, degree of modification: 25 %) were provided by an industrial source. Acetone was purchased from Sigma Aldrich (Gillingham, UK). Sodium hydroxide (NaOH) (laboratory reagent grade) and hydrochloric acid (HCl) (laboratory reagent grade, 37 %) were purchased from Fisher Scientific (Loughborough, UK). DI water (18.2 MΩ cm) was produced using a Direct-Q 3 UV water purification system (Merck, Darmstadt, Germany).

OCNF gel production and modification

The OCNF gel was diluted down to approx. 1.6 wt.% using DI water before being passed through an APV-2000 laboratory homogenizer (SPX FLOW, Sussex, UK) seven times (pressures of 700, 1030, 1220, 1540, 1490, 1540 and 1530 MPa respectively). The suspension was cooled on ice between each pass. The suspension was then placed in dialysis membrane and concentrated to 4 wt.% for the concentration experiments and 5 wt.% for the pH experiments at ambient temperature in a fume hood.

For the pH modified samples, solutions of HCl and NaOH at concentrations of 2×10^{-1}, 2×10^{-2}, 2×10^{-3}, 2×10^{-4}, 2×10^{-5}, 2×10^{-6}, and 2×10^{-7} M were produced using DI water. These were then mixed with the 5 wt.% OCNF gel in a 1:1 weight ratio to give a series of 2.5 wt.% OCNF gels with equivalent aqueous pH values ranging from 1 to 13. Finally, these were ultrasonicated using a digital sonifier 450 (Branson Ultrasonics Corporation, Connecticut, USA) for 5 min (10 % power, 30 s power followed by 30 s rest on ice).

OCNF macrofiber production

A 2.5 wt.% OCNF gel was extruded into an acetone bath using a pump 11 elite syringe pump (Harvard Apparatus, Holliston, US) (extrusion rate: 0.3 mL min^{-1}, needle gauge: 21). This was collected onto a glass cylinder before being allowed to dry at R.T. to generate a macrofibre consisting of entangled OCNFs.

ζ-potential

The OCNF gels were further diluted to 0.05 wt.% using the respective HCl, or NaOH, solution and DI water in a 1:1 volumetric ratio. These were ultrasonicated again for 2 min (10 % power, 30 s power followed by 30 s rest on ice) prior to measurement. The ζ-potentials were measured using a Zetasizer Nano ZS (Malvern Panalytical, Surrey, UK). Five repeats were measured for each sample.

Rheometry

All gel rheological tests were performed with a TA Discovery Hybrid HR-1 rheometer (TA Instruments, New Castle, USA). A cone (angle: 4°, diameter: 40 mm) geometry was selected. Testing was carried out at a constant temperature of 25 °C. Angular frequency sweeps were performed between 0.4 and 600 rad s^{-1} at a constant strain of 1.0 %.

Raman spectroscopy

Raman spectra were acquired using a confocal Raman microscope (Alpha300, WITec GmbH). The spectrometer was equipped with a UHTS 300 VIS spectrometer and a thermoelectrically cooled CCD detector (down to -62 °C), with an 1800 g mm^{-1} grating. A 532 nm wavelength laser (VIS) was used for excitation, and a 50× objective lens was used for the backscattered light collection. Single Raman spectra were recorded using an exposure time of 10 s and twenty-five accumulations. The average of three single spectra were used for analysis.

WITec Project Plus and Origin-Pro software were used to analyse Raman spectra. First, cosmic ray removal and back-ground subtraction were performed using WITec Project Plus. The fitting of the Raman bands at ~1100, 1645, and 1725 cm^{-1} was conducted using Origin-Pro software.

Small angle X-ray scattering (SAXS)

SAXS measurements were performed on an Anton-Paar SAXSpoint 2.0 equipped with a copper source (Cu Kα, λ = 1.542 Å) and a 2D EIGER R series Hybrid Photon Counting (HPC) detector. The sample-to-detector distance was 556 mm covering a range of the scattering vector (q) of approx. $0.06 < q < 4$ $Å^{-1}$. Samples were loaded into 1 mm quartz capillaries, and

the scattering intensity (I(q)) was collected in three frames, with 300 s exposure per frame. Temperature was kept at 25 °C via a Peltier unit (±0.1 °C). Kratky plots (I(q).q^2 vs. q) were generated for each sample after background subtraction. Gaussian curves were fitted to the plots using Fityk to determine fibril spacings and relative contributions.

Multi-channel confocal laser scanning spectroscopy (MCLSS)

Spectral images were acquired using a Zeiss LSM 880 confocal microscope (405 nm diode laser, 5.0 % power, Plan-Apochromat 10×/0.45 M27 objective, MBS-405 filter, 32 channels: λ = 411-695 nm). Spectral analysis was performed using the unmixing tool in ZEN 2.6 (blue edition) (Carl Zeiss AG, Oberkochen, Germany). Three images were acquired for each condition. These were sectioned into fifths and spectra for each section obtained, which were then averaged for each image. For the concentration data, measurements were reproduced three times at each concentration using different OCNF gels. For the pH data, measurements were reproduced four times at each pH using different OCNF gels.

For the macrofibre expansion experiment, a fibre was held in place using carbon tape. Water (500 µL) was added after 7 s. The experiment was conducted for 30 min, with a spectral image acquired every 0.52 s. Images were processed as before to obtain spectral data. The fibre diameter was estimated using Fiji. Briefly, images were converted to 8-bit before automatic thresholding. An ellipse was fitted to the threshold area and the minor axis determined.

Results & Discussion

Under excitation at 405 nm, the emission spectra for CNMs, such as OCNFs (Figure 1a) and CNCs,[35] appear to have two dominant emission wavebands centred at 468 and 504 nm. The excitation/emission shift observed for the first band is the same as that reported by Gong *et al*. (emission maxima at 427 nm under excitation at 365 nm),[29] for native cellulose. This indicates that the fluorescence band observed at 468 nm is due to the overlap of oxygen orbitals and can be assigned to the intra-CNM interactions. Similarly, Li *et al*. reported a redshift of 40 nm between the first and second bands,[33] which matches that observed in our analysis. Therefore, the band at 504 nm can be assigned to transitions involving the π* orbitals of the surface groups (carboxyl groups for OCNF and sulfate half esters for CNCs) and will be dependent on inter-CNM interactions. It is noted that the emission wavelength is independent of the excitation wavelength in conventional fluorophores. However, the excitation/emission matrix for cellulose reported by Pöhlker *et al*. clearly shows emission maxima that exhibit a linear dependence on the excitation wavelength.[28] This can be attributed to the presence of multiple possible energy bandgaps due to the range of unique orbital overlaps arising from the complex nature of the bonding and molecular forces in saccharides, as suggested by Zhou *et al*.[39]

Consequently, as the CNM concentration initially increases, the intensity due to the increasing number of interparticle interactions relative to the number of particles. Considered

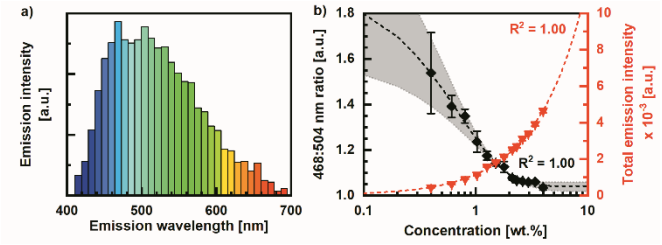

Figure 1. a) Typical emission spectrum of 4 wt.% OCNF gel excited at 405 nm. b) Primary axis: change in 468:504 nm band emission intensity ratio (black diamonds) with respect to OCNF concentration. Exponential function (Equation 4) fitted to mean data values (dashed black line). Upper and lower bound region (shaded area between dotted grey lines) determined by fitting function to mean data values ± SE (Table S1). Secondary axis: change in total emission intensity (red inverted triangles) with respect to OCNF concentration. Linear function fitted to mean data values (red dashed line). N = 3, n = 3. Error bars: ± SE.

from a mathematical perspective, the intensity of the 468 nm band will be directly proportional to the number of CNMs present within a given volume, *i.e.* the crowding number (n_{crowd}), which can be related to the aspect ratio (A) and the fibre volume density (c_{vol}):

$$n_{crowd} = {}^{2}/_{3}\ A^2.c_{vol} \quad (1)$$

assuming a spherical volume with a diameter equal to the fibre length (λ) and that the CNMs can be modelled as stiff rods.[40] Based the fibre contact number,[41] the 504 nm band intensity will be dependent on the number of fibre interactions within the volume ($n_{interact}$):

$$n_{interact} = A.c_{vol}.n_{crowd} \quad (2)$$

As the CNM concentration ([CNM]) tends to 0 wt.%, c_{vol} will also tend to zero, equation 3:

$$[CNM] \rightarrow 0\ wt.\%, c_{vol} \rightarrow 0;$$

$$[CNM] \rightarrow 100\ wt.\%, c_{vol} \rightarrow c_{vol(\max)} \quad (3)$$

assuming that the fibres are well dispersed within the volume. Conversely, as [CNM] approaches 100 wt.%, c_{vol} will approach a maximum value, often assumed to be within 20 % of the density of pure crystalline cellulose (1582-1599 kg m^{-3} for type I).[42]

The change in the ratio between the two bands should plateau once $n_{interact}$ reaches its maximum, assumed to be at $c_{vol(max)}$ for a system where CNMs are randomly distributed. However, for systems where long-range CNM interactions result in ordering of the system, such as liquid crystals, $n_{interact}$ will not be independently affected by c_{vol}, i.e. Equation 2 will simplify to Equation 4. Further increases in c_{vol} will result in an increase in the packing density without increasing the number of interactions observed by a single CNM.

$$n_{interact} = A.n_{crowd} \quad (4)$$

This theory was previously used to accurately predict the concentration at which the chiral nematic phase of a CNC suspension forms and the CAC of hydrophobized CNCs,[35] both of which could be reasonably assumed to be inflexible spherocylinders due to their highly crystalline structure.[1,2] Comparatively, OCNFs have higher aspect ratios and consist of multiple crystalline and disordered domains, resulting in flexible

chains that impact the concentration at which interactions occur and their ability to pack.[43] To confirm this, the effect of OCNF concentration on the emission intensity ratio between the bands centred at 468 and 504 nm was probed using MCLSS (Figure 1b).

As observed with CNCs,[35] the ratio between the two bands initially decreased as concentration increased, indicating an increase in the interaction between the nanofibrils, before plateauing. Calculation of the interception point between the initial and final gradients of a fitted exponential curve (Equation 5):

$$y = Ae^{(1-Bx)} + C \quad (5)$$

where A, B, and C are constants, determined a CAC of 1.5 ± 0.1 wt.% (Table S1), which is comparable to the reported OCNF gelation point between 1.5 and 2.0 wt.%,[45] and reflects the concentration at which liquid crystalline domains are observed (Figure S1). In comparison, the CACs of sulfated and hydrophobic CNCs were correspondingly reported to be 3.3 and < 0.3 wt.%.[35] The increased length and flexibility of the OCNFs result in them interacting with one another at a lower concentration than the CNCs. This is supported by sedimentation experiments to determine aspect ratio, whereby higher aspect ratios result in lower gelation concentrations.[44] However, OCNFs are still hydrophilic and have an anionic surface charge that inhibits their aggregation.[43,45,46] Therefore, a higher concentration is required for gelation than for hydrophobic CNCs, which rapidly cluster together with a poor packing structure.[35]

The continued increase in fluorescent intensity (Figure 1b) beyond the gelation point provides further proof that conventional fluorophores, which quench upon aggregation, are not the source of the observed photoluminescence. This has also been previously observed in synthetic, carbonyl-containing polymer hydrogels,[47] further supporting the theories presented here.

Prior to determining the potential impact of protonation on the autofluorescent spectra, three techniques (ζ-potential, Raman spectroscopy, and rheology) were used to understand the effect of change in pH on the OCNF microenvironment (Figure 2, Table 1). It is challenging to precisely measure the pH of a gel system. Therefore, the data obtained was plotted against the equivalent aqueous pH, enabling a continuous ordinate axis, rather than against the molar concentration of HCl, or NaOH, added (Figure S2). To determine whether the buffering effect of the OCNFs would impact the predicted interception points, the ζ-potential measurements of the 0.02 wt.% OCNF suspension were plotted against both the equivalent aqueous pH and the measured OCNF suspension pH (Figure S3, Table S2 and S3). No significant difference was observed between the calculated interception points, and the average acidic interception point value of 3.7 ± 0.1 (Table 1) is close to the previously reported apparent pKa value of 3.9 for the carboxyl groups present in OCNFs.[48] This latter result is expected as the pH tends from 7 to 1; as the carboxyl group protonates, the ζ-potential will increase due to the decreasing anionic surface charge (Figure 2a and S3).

Table 1. Calculated interception points from ζ-potential, Raman spectroscopy and rheology techniques, and their average. Data used to determine the interception points may be found in the supplementary information (Table S2, S6, S7, and S8). Error: ± SE.

Analytical technique		Interception point	
		Acidic	Basic
ζ-potential	Equivalent aqueous pH	3.4 ± 0.1	10.7 ± 0.1
Raman Spectroscopy	1725:1100 ratio	3.9 ± 0.1	10.3 ± 0.2
	1645:1100 ratio	3.9 ± 0.2	-
Rheology	Intrinsic G'	3.5	10.4
	Intrinsic G"	4.0	10.7
Average of techniques		3.7 ± 0.1	10.5 ± 0.1

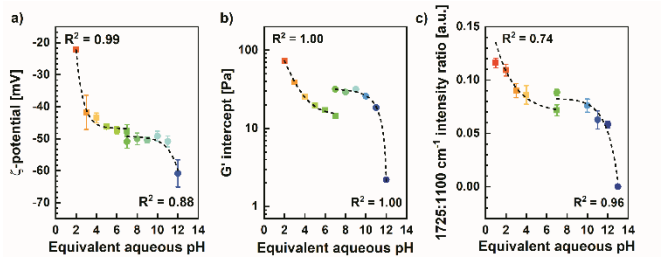

Figure 2. a) Effect of pH variation on ζ-potential of 2.5 wt.% OCNF gel. b) Effect of pH variation on hydrogen bonding with carboxyl groups present in OCNF gel as determined by Raman spectroscopy. c) Effect of pH variation on the intrinsic storage modulus of 2.5 wt.% OCNF gel as determined by rheology. HCl (squares) and NaOH (circles) used to modify gels. Equation 4 fitted to data to produce lines of best fit. Error bars: ± SE.

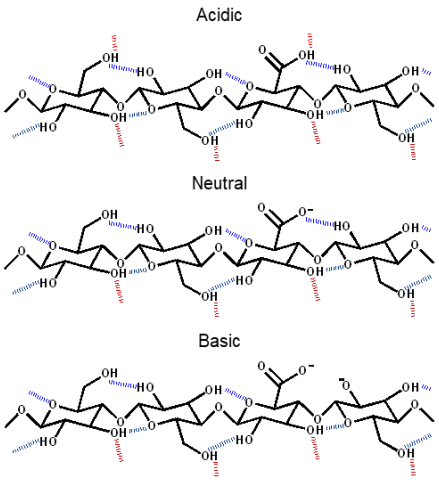

Figure 3. Representative interactions of a model glycan chain at the OCNF surface under varying pH conditions. Under acidic conditions, protonation of the carboxyl group reduces electrostatic repulsion leading to aggregation of the fibrils and the presence of interfibril molecular forces (van der Waals, hydrogen bonding) (bright red hashed lines). Under neutral conditions, carboxyl group deprotonation results in domination of electrostatic interaction, increasing the fibril distances and minimizing the contribution of interfibril molecular forces. Under basic conditions, surface intrachain hydrogen bonds (bright blue hashed lines) with the carboxyl group are lost and an increase in electrostatic repulsion between fibrils is observed. Intrafibril molecular forces (dull red and blue hashed lines) are unaffected by changes in pH.

Protonation results in the aggregation of the OCNF gel due to the loss of electrostatic charge,[46,49] leading to an increase in distances between fibrils that are shorter than the sum of the van der Waals radii as determined by SAXS (Figure S4, Table S4 and S5). This increases the contribution from van der Waals forces and hydrogen bonding between the fibrils (Figure 3), resulting in an increase in the intrinsic storage and loss moduli

as determined by angular frequency sweeps (Figure 2b and S5). In addition, Raman spectroscopy (Figure 2c and S6a), reveals an increase in the band at ~1725 cm^{-1}, which relates to carboxyl group hydrogen bonding,[50] comparative to the band at ~1100 cm^{-1}, attributed to C-O-C bonding,[50,51] which will be unaffected by pH. This suggests that these interfibrillar interactions could involve hydrogen bonds. This is further supported via comparison of the Raman band located at ~1645 cm^{-1} – which relates to either the presence of surface bound water, or the deprotonated form of the carboxyl group – to the band located at ~1100 cm^{-1} (Figure S6c).

The differences observed in the experimental properties between the addition of HCl and NaOH under neutral conditions is attributed to the Hoffmeister effect.[52] Given that previous studies suggest that the pKa values for the hydroxyl groups in cellulose are greater than 12,[53-55] it is unexpected that a second interception point at pH 10.5 is observed for all three techniques (Figure 2, Table 1). The decrease in ζ-potential (Figure 2a) indicates that deprotonation is occurring, although it is unlikely to be all the hydroxyl groups present on the fibril surface as the decrease is less than that for deprotonation of the carboxyl group, which accounts for only 25 % of the C6 functional groups. The decrease in the 1725:1100 cm^{-1} ratio observed by Raman spectroscopy (Figure 2c) suggests that it is the hydroxyl groups (presumed to be C2 in Figure 3) that form intrachain hydrogen bonds with the carboxyl group that deprotonate. The resulting increase in repulsion between fibrils minimises interfibrillar interaction, observed as a further decrease in the gel's storage and loss moduli (Figure 2b and S4). No change is observed in the 1645:1100 cm^{-1} ratio (Figure S6c) as the carboxyl group is already completely deprotonated and water accessibility does not change.

MCLSS was used to probe the effect of pH on the OCNF gel autofluorescent spectra (Figure 4a). Two features are noted. Firstly, as the pH becomes more basic, the emission intensity of the band at 504 nm increases, leading to its dominance over the band at 468 nm. Secondly, the 468 nm remains the dominant band over the two bands on either side irrespective of pH value, whilst the 513 nm band becomes dominant over the 504 nm band as the pH tends to 13.

Plotting the intensity ratio between the 468 and 504 nm bands reveals an increase as protonation events occur (Figure 4b). The decrease observed at pH 1, and large error bars at pH 2 relative to the other values, is likely due to aggregation (Figure S7), which results in a decrease in the ratio due to the effective increase in concentration (Figure 1b), although no significant change is observed in the total emission intensity (Figure S8). It is expected that no change would be observed for the 468 nm ratio relative to the immediate bands either side as it arises from molecular interactions within the fibrils. Therefore, it will not be affected by changes in the surface environment. For the 504:513 nm ratio, a decrease is observed under basic conditions, confirming the association of the peak with the surface carboxyl groups. Importantly, the calculated interception points for the 468:504 and 504:513 nm ratios (3.7 ± 0.3 and 10.4 ± 0.1, and 10.5 ± 0.3 respectively) are not significantly different from the averages determined from the

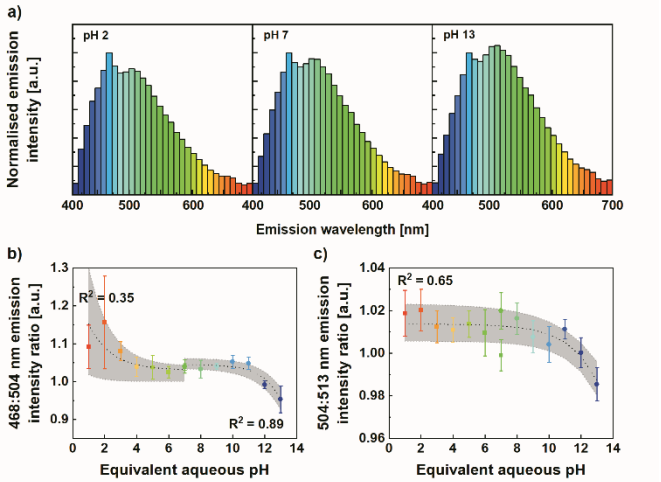

Figure 4. a) Variation in the OCNF gel emission spectrum with pH as measured using MCLSS. Normalised to 468 nm emission intensity. b) Variation of the ratio between 468 and 504 nm band intensities with gel pH. c) Variation of 504:513 nm intensity ratio with gel pH. Exponential functions (Equation 4) fitted to mean data values (dashed black line). Upper and lower bound region (shaded area between dotted grey lines) determined by fitting function to mean data values ± SE (Table S9 and S10). HCl (squares) and NaOH (circles) used to modify gels. N = 4, n = 3. Error bars: ± SE.

other techniques (Table 1), confirming the role of protonation, and resultant changes in molecular forces, in the fluorescent mechanism.

Aggregation of the fibrils, leading to an increase in concentration, under acidic conditions may contribute to the increase in the 468:504 nm ratio, but this is counter to the changes observed in the prior concentration experiments as the number of interactions observed will also increase. Therefore, it is more likely that changes in the molecular forces experienced by the carboxyl group impacts the molecular distances and angles between it and the oxygen groups involved in the n,π* transitions, affecting the emission intensity of the 504 nm band. These two parameters have previously been identified by Li *et al*. as being instrumental in the formation of suitable pathways for photoluminescence.[33] Investigations into this are, however, not within the scope of this paper.

The ability of the MCLSS to generate 512×512 pixel maps at almost 2 fps gives it a distinct advantage for providing time dependent, spatially resolved chemical information over other spectroscopic techniques, such as Infrared and Raman. To demonstrate the effects of both protonation and concentration on fluorescence in a rapidly changing environment, a dry macrofibre produced by extruding an OCNF gel into an acetone bath was immersed in water, resulting in its expansion (Figure 5a). The resultant 468:504 nm ratio plotted against time (Figure 5b) reveals an initial rapid decrease (within 5 s) in the ratio upon addition of water, followed by a slow increase over the next half an hour to a value greater than that observed in the dry state. Based on the previous experiments, the initial ratio decrease can be attributed to deprotonation of the carboxyl group upon the introduction of water. The subsequent increase in the fibril surface charge causes the fibrils to repel one another, resulting in an initial rapid expansion of the macrofibre (Figure 5c). The concurrent increase in the total emission intensity is theorised

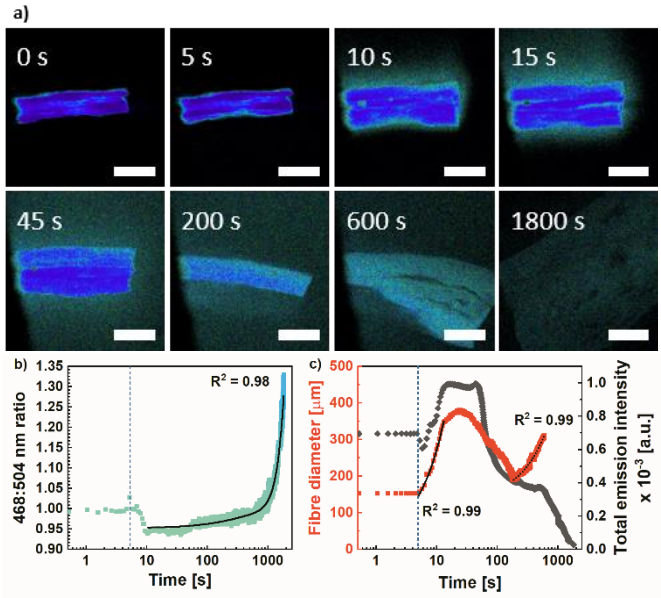

Figure 5. a) Select stills from MCLSS video (available in SI) of OCNF macrofibre expansion upon immersion in water. Scale bar: 200 µm b) 468:504 nm emission intensity ratio of OCNF macrofibre against time. Water added at approximately 5 s (blue dashed line). Third order polynomial fitted to data after 11 s (solid line) c) Total emission intensity and fibre diameter against time. Initial expansion gradient (dotted line) 85 times greater than final expansion gradient (solid line) Between ~30-200 s fibre movement out of the focus plane results in apparent decrease in diameter. After ~600 s, the fibre diameter is greater than the viewing window, resulting in inaccurate diameter data and an increase in the rate of emission intensity decrease.

to be primarily due to an increase in the observed image fraction that is fluorescent whilst maintaining a high concentration, minimising the effect of concentration on intensity. After this initial expansion, the OCNFs enter a more gradual dispersive phase (fitted gradient over 85 times shallower than that of the initial expansion (Figure 5c)), decreasing their concentration, observed as an increase in the 468:504 nm ratio and decrease in emission intensity. After half an hour, the OCNF concentration at the point of the original fibre is ~1 wt.% (Figure 1b, 5b). Retention of the macrofibre structure is observed despite the low concentration (Figure 5a).

Conclusions

Based on the works of Gong *et al*. and Li *et al*. regarding the autofluorescence of polysaccharides and cellulose nanofibril surface groups, we hypothesise that ratios between the two fluorescent bands can be used to track changes in the CNM physicochemical environment. We confirm that the critical aggregation concentration can be determined at the point where the band intensity ratio becomes independent of the concentration. We also demonstrate that protonation/ deprotonation of the fibril surface results in ratio shifts due to the resulting changes in molecular forces only affecting one band, although further research is required to fully understand the mechanisms behind this. Finally, the applicability of MCLSS to track these changes in the OCNF physicochemical environment at almost 2 fps has been demonstrated via the dispersion of a dry OCNF macrofibre in water. We envisage that the technique will prove complimentary to IR and Raman spectroscopy in static situations, able to probe interchain interactions between specific chemical groups. In addition, it presents future opportunities for rapidly probing CNM interactions with their environment and other materials in dynamic situations over an area and time frame that other spectroscopy techniques would be unable to track.

Conflicts of interest

There are no conflicts to declare.

Acknowledgements

The authors would like to thank the Engineering and Physical Sciences Research Council (EPSRC) for provision of financial support grant no. (EP/N03340X/2). They gratefully acknowledge Dr Zakir Hossain at the University of Bath for help with SAXS acquisition, and the Material and Chemical Characterisation Facility (MC^2) at the University of Bath, http://go.bath.ac.uk/mc2, for their support and assistance in this work with regards to MCLSS.

References

1 R.J. Moon, A. Martini, J. Nairn, J. Simonsen, J. Youngblood, *Chem. Soc. Rev.* 2011, **40**, 3941.
2 K.J. De France, T. Hoare, E.D. Cranston, *Chem. Mater.* 2017, **29**, 4609.
3 A. Dufresne, *Mater. Today* 2013, **16**, 220.
4 A.N. Nakagaito, H. Yano, *Appl. Phys. A* 2004, **78**, 547.
5 M.E. Malainine, M. Mahrouz, A. Dufresne, *Compos. Sci. Technol*. 2005, **65**, 1520.
6 C. Palange, M.A. Johns, D.J. Scurr, J.S. Phipps, S.J. Eichhorn, *Cellulose* 2019, **26**, 9645.
7 H. Kargarzadeh, M. Mariano, J. Huang, N. Lin, I. Ahmad, A. Dufresne, S. Thomas, *Polymer* 2017, **132**, 368.
8 H. Yu, C. Yan, J. Yao, *RSC Adv.* 2014, **4**, 59792.
9 J. Wang, D.J. Gardner, N.M. Stark, D.W. Bousfield, M. Tajvidi, Z. Cai, *ACS Sustain. Chem. Eng.* 2018, **6**, 49.
10 J.K. Jackson, K. Letchford, B.Z. Wasserman, L. Ye, W.Y. Hamad, H.M. Burt, *Int. J. Nanomed*. 2011, **6**, 321.
11 O.L. Galkina, V.K. Ivanov, A.V. Agafonov, G.A. Seisenbaeva, V.G. Kessler, *J. Mater. Chem. B* 2015, **3**, 1688.
12 R.M.A. Domingues, M.E. Gomes, R.L. Reis, *Biomacromolecules* 2014, **15**, 2327.
13 A. Khan, Y. Wen, T. Huq, Y. Ni, *J. Agric. Food Chem*. 2018, **66**, 8.
14 J. Araki, M. Wada, S. Kuga, T. Okano, *Colloids Surf. A* 1998, **142**, 75.
15 B.G. Rånby, *Acta Chem. Scand.* 1949, **3**, 649.
16 B.G. Rånby, *Discuss. Faraday Soc*. 1951, **11**, 158.
17 R.H. Marchessault, F.F. Morehead, M.J. Koch, *J. Colloid Sci.* 1961, **16**, 327.
18 H. Sadeghifar, I. Filpponen, S.P. Clarke, D.F. Brougham, D.S. Argyropoulos, *J. Mater. Sci.* 2011, **46**, 7344.
19 M. Usuda, O. Suzuki, J. Nakano, N. Migita, *J. Soc. Chem. Ind*., Japan 1967, **70**, 349.
20 S. Camarero Espinosa, T. Kuhnt, E.J. Foster, C. Weder, *Biomacromolecules* 2013, **14**, 1223.
21 O.M. Vanderfleet, D.A. Osorio, E.D. Cranston, *Philos. Trans. Royal Soc. A* 2017, **376**, 20170041.

22 S. Spinella, A. Maiorana, Q. Qian, N.J. Dawson, V. Hepworth, S.A. McCallum, M. Ganesh, K.D. Singer, R.A. Gross, *ACS Sustain. Chem. Eng*. 2016, **4** (3), 1538.
23 H.-Y. Yu, D.-Z. Zhang, F.-F. Lu, J. Yao, *ACS Sustain. Chem. Eng*. 2016, **4**, 2632.
24 L. Chen, J.Y. Zhu, C. Baez, P. Kitin, T. Elder, *Green Chem.* 2016, **18**, 3835.
25 A. Isogai, T. Saito, H. Fukuzumi, *Nanoscale* 2011, **3**, 71.
26 A. Isogai, T. Hänninen, S. Fujisawa, T. Saito, *Prog. Polym. Sci.* 2018, **86**, 122.
27 J.A. Olmstead, D.G. Gray, D. G., *J. Photochem. Photobiol. A*, 1993, **73**, 59.
28 C. Pöhlker, J.A. Huffman, U. Pöschl, *Atmos. Meas. Tech*. 2012, **5**, 37.
29 Y.Y. Gong, Y.Q. Tan, J. Mei, Y.R. Zhang, W.Z. Yuan, Y.M. Zhang, J.Z. Sun, B.Z. Tang, *Sci. China: Chem*. 2013, **56** (9), 1178.
30 M.A. Johns, Y. Bae, F.E.G. Guimarães, E.M. Lanzoni, C.A.R. Costa, P.M. Murray, C. Deneke, F. Galembeck, J.L. Scott, R.I. Sharma, *ACS Omega* 2018, **3**, 937.
31 M.A. Johns, A.E. Lewandowska, S.J. Eichhorn, *Microsc. Microanal*. 2019, **25**, 682.
32 L.-L. Du, B.-L. Jiang, X.-H. Chen, Y.-Z. Wang, L.-M. Zou, Y.-L. Liu, Y.-Y. Gong, C. Wei, W.-Z. Yuan, *Chinese J. Polym. Sci.* 2019, **37**, 409.
33 M. Li, X. Li, X. An, S. Chen, H. Xiao, *Front. Chem*., 2019, **7**, 447.
34 Y. Yu, S. Gim, D. Kim, Z.A. Arnon, E. Gazit, P.H. Seeberger, M. Delbianco, *J. Am. Chem. Soc*. 2019, **141**, 4833.
35 R. Nigmatullin, M.A. Johns, J.C. Muñoz García, V. Gabrielli, J. Schmitt, J. Angulo, Y.Z. Khimyak, J.L. Scott, K.J. Edler, S.J. Eichhorn, *Biomacromolecules* 2020, DOI: 10.1021/acs.biomac.9b01721
36 I.A. Sacui, R.C. Nieuwendaal, D.J. Burnett, S.J. Stranick, M. Jorfi, C. Weder, E.J. Foster, R.T. Olsson, J.W. Gilman, *ACS Appl. Mater. Interfaces*, 2014, **6**, 6127.
37 H. Zhang, Z. Zhao, P.R. McGonigal, R. Ye, S. Liu, J.W.Y. Lam, R.T.K. Kwok, W.Z. Yuan, J. Xie, A.L. Rogach, B.Z. Tang, *Mater. Today* 2020, **32**, 275.
38 W.Z. Yuan, Y. Zhang, *J. Polym. Sci. A* 2017, **55**, 560.
39 Q. Zhou, T. Yang, Z. Zhong, F. Kausar, Z. Wang, Y. Zhang, W.Z. Yuan, *Chem. Sci*. 2020, **11**, 2926.
40 R.J. Kerekes, C.J. Schell, *J. Pulp Pap. Sci.* 1992, **18**, 32.
41 O. Kallmes, H. Corte, *Tappi* 1960, **43**, 737.
42 J. Sugiyama, R. Vuong, H. Chanzy, *Macromolecules* 1991, **24**, 4168.
43 J. Schmitt, V. Calabrese, M.A. da Silva, S. Lindhoud, V. Alfredsson, J.L. Scott, K.J. Edler, *Phys. Chem. Chem. Phys*. 2018, **20**, 16012.
44 S. Varanasi, R. He. W. Batchelor, *Cellulose* 2013, **20**, 1885.
45 R.J. Crawford, K.J. Edler, S. Lindhoud, J.L. Scott, G. Unali, *Green Chem*. 2012, **14**, 300.
46 L. Mendoza, W. Batchelor, R.F. Tabor, G. Garnier, *J. Colloid Interface Sci.* 2018, **509**, 39.
47 H-X. Xu, Y. Tan, D. Wang, X-L. Wang, W-L. An, P-P. Xu, S. Xu, Y-Z. Wang, *Soft Matter* 2019, **15**, 3588.
48 M. Spaic, D.P. Small, J.R. Cook, W. Wan, *Cellulose* 2014, **21**, 1529.
49 A.B. Fall, S.B. Lindström, O. Sundman, L. Ödberg, L. Wågberg, *Langmuir*, 2011, **27**, 11332.
50 G. Socrates, *Infrared and Raman Characteristic Group Frequencies: Tables and Charts*, John Wiley & Sons Ltd, Chichester, 2004.
51 U.P. Agarwal, *Molecules* 2019, **24**, 1659.
52 N. Vlachy, B. Jagoda-Cwiklik, R. Vácha, D. Touraud, P. Jungwirth, W. Kunz, *Adv. Colloid Interface Sci*. 2009, **146**, 42.
53 E. Gaidamauskas, E. Norkus, E. Butkus, D.C. Crans, G. Grinciene, *Carbohydr. Res*. 2009, **344**, 250.
54 S. Feng, C. Bagia, G. Mpourmpakis, G., *J. Phys. Chem. A* 2013, **117**, 5211.
55 E. Bialik, B. Stenqvist, Y. Fang, Å. Östlund, I. Furó, B. Lindman, M. Lund, D. Bernin, *J. Phys. Chem. Lett.* 2016, **7**, 5044.